



Viscoelasticity effects on hydrodynamic characteristics of electrokinetically driven flow in rectangular microchannels

M.M. Heydari*

Propulsion Group, Aerospace complex, Malek-Ashtar University of Technology, Tehran, Iran.

Received 10 July 2014; received in revised form 6 October 2014; accepted 1 December 2014

KEYWORDS

Electroosmotic flow;
Microfluidics;
Numerical modeling;
PTT model;
FENE-P model.

Abstract. The biomicrofluidic devices utilizing electroosmosis for flow actuation are usually encountered with non-Newtonian behavior of working fluids. Hence, studying the flow of non-Newtonian fluids under an electroosmotic body force is of high importance for accurate design and active control of these devices. In this paper, mixed electroosmotically and pressure driven flow of two viscoelastic fluids, namely PTT and FENE-P models, through a rectangular microchannel is examined. The governing equations in dimensionless form are numerically solved through a finite difference procedure for a non-uniform grid. It is observed that although the Debye-Hückel linearization fails to predict the velocity profile for viscoelastic fluids, this approximation holds even at high zeta potentials, provided the velocity field is normalized with the mean velocity. It is also revealed that the dependency of the mean velocity on the level of elasticity in the fluid is linear. This functionality results in a Poiseuille number independent of the level of elasticity in the fluid. Moreover, the pressure effects are pronounced for higher values of the channel aspect ratio. In addition, both the mean velocity and the Poiseuille number are increasing functions of the channel aspect ratio.

© 2015 Sharif University of Technology. All rights reserved.

1. Introduction

Electrokinetics is a term classically used for referring to any motion which is created due to the interaction of ionic clouds, charged surfaces, and electric fields. With the exploration of dielectrophoresis, this classical definition has encountered a real challenge, because this phenomenon is a result of applying non-uniform electric fields and does not require ionic solutions to take effect [1]. Given the characteristics of dielectrophoresis, a better definition of electrokinetics may be given to be any kind of motion which is created due to the presence of macroscopic electric fields.

Having been explored more than two centuries

ago [2], electroosmosis is one of the first electrokinetic phenomena to be discovered. Electroosmosis refers to flow actuation by applying an electric field to an electrolyte solution in contact with a surface. The contact of the surface with the electrolyte solution results in the formation of an Electric Double Layer (EDL), shown in Figure 1, within which there is a net charge density. Therefore, the application of an external electric field can result in a net flow toward the cathode or anode, depending on the sign of the charge density.

In spite of a long history, it took a long time for electroosmosis to be widely used in practice. The main difficulty associated with the commercialization of electroosmosis was that it requires small length scales to take effect. Hence, considerable progresses, in this respect, were only become possible after major

*. Tel.: +98 21 66065030;
E-mail address: mmheydari@gmail.com

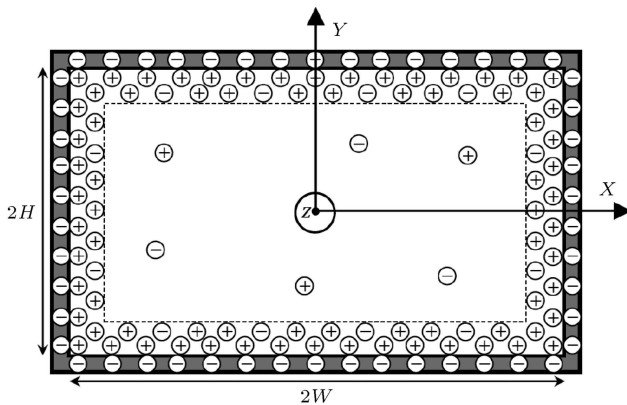


Figure 1. Schematic of the physical problem along with the coordinate system. EDLs are the regions between the dashed lines and the channel wall [21].

advancements in microfabrication technology in the late 20th century which led to the development of various microfluidic devices. Among these microdevices are various types of microthrusters including miniaturized electrokinetic thrusters [3] developed for space propulsion. Another microdevice in which electroosmosis plays an important role is a Lab-On-a-Chip (LOC) system. Lab-on-chip devices are microscale laboratories on a microchip that can perform medical diagnoses. The main advantages of these devices are ease of use, speed of analysis, and low sample consumption. Electroosmosis is the main mechanism for flow generation in lab-on-chip devices. Electroosmotic micropumps have many advantages over other types of micropumps. For example, though the head produced by conventional pumps should increase with decreasing the channel diameter to overcome the extra pressure drop, the maximum electroosmotic velocity is not dependent upon the channel diameter. Furthermore, the electroosmotic pumps are bidirectional, can generate constant and pulse free flows with flow rates well suited to lab-on-chip devices, and can be readily integrated with them [4].

The study of liquid flow in microchannels with consideration of electrokinetic effects can be traced to 1960s. The early analytical works on electroosmotic flow report the electrokinetically driven fully developed flow in slit and cylindrical microchannels [5-7]. More recently, Tsao [8] analyzed the hydrodynamic features of electroosmotic flow in a microannulus. He developed analytical solutions for potential and velocity distributions, using the Debye-Hückel linearization. The above work was extended to high zeta potentials by Kang et al. [9], using an approximate method. Analytical solutions for fully developed electroosmotic flow in rectangular and semicircular microchannels were presented by Yang [10] and Wang et al. [11], respectively. Wang and Chang [12] developed an efficient Ritz method from the variational principle to solve the

Poisson-Boltzmann equation under the Debye-Hückel approximation for studying the electroosmotic flow in microchannels. The method was then applied to the family of super elliptic cross sections which includes the elliptic and rectangular channels as limiting cases. More complex geometries were considered by Goswami and Chakraborty [13] and Vocale et al. [14].

An understanding of the flow characteristics of common biofluids is crucial in design and active control of LOCs. Because of complex structure, common biofluids such as blood, saliva, and synovial fluid usually show non-Newtonian rheological behaviors. Therefore, any related study should account for these complex behaviors. The available literature indicates a growing interest in modeling of the non-Newtonian electroosmotic flow in recent years. One of the first attempts in this context was carried out by Das and Chakraborty who derived analytical solutions for the transverse distributions of velocity, temperature and solutal concentration in electroosmotic flow of power-law fluids through a slit by means of an approximate method [15]. Zhao and coworkers [16,17] obtained expressions for the Helmholtz-Smoluchowski electroosmotic velocity of power-law fluids at small and high zeta potentials. By means of the same non-Newtonian model, Vasu and De [18] analyzed the electroosmotic flow in a slit microchannel at high zeta potentials. Lattice Boltzmann based numerical studies of the electroosmotic flow of power-law were conducted by Tang et al. [19,20]. In a recent study, Vakili et al. [21] studied the electroosmotic flow of power-law fluids in a rectangular microchannel.

The viscoelastic constitutive equations have also received much attention in electrokinetics studies. Park and Lee [22] devised a simple method based on the concept of the Helmholtz-Smoluchowski velocity to find the volumetric flow rate of viscoelastic electroosmotic flows through microchannels. The electroosmotic flow of viscoelastic fluids through parallel plate microchannels was analytically investigated by Dhinakaran et al. [23]. Analytical solutions were presented by Afonso et al. [24] for the flow of viscoelastic fluids through parallel plates and pipes under the combined influence of electrokinetic and pressure forces. In addition, these authors recently reported a finite volume based numerical study on electroosmotic flow in a cross slot using the same rheological model [25]. Another work of this research group is dealing with the two fluid electroosmotic flow of viscoelastic fluids [26]. Sousa et al. [27] derived analytical solutions for mixed electroosmotic and pressure driven flow of viscoelastic fluids by taking into account the near-wall depletion of macromolecules. More recent works have also been reported regarding electroosmotic flow of viscoelastic fluids [28-31].

Microfluidic circuits are usually produced by

etching on a substrate, so that the channel cross-sections are generally trapezoidal or rectangular in shape [32]. However, to the author's best knowledge, no study has been undertaken on electroosmotic flow of viscoelastic fluids in either of these geometries. The objective of this paper is to extend the previous studies on electroosmotic flow of viscoelastic fluids by considering a rectangular geometry. Through this line, both PTT and FENE-P models are being considered, assuming a hydrodynamically developed flow. The governing equations are first made dimensionless and then transformed into new ones based on the computational parameters which provide mesh clustering near the wall. Afterward, the transformed equations are discretized using a finite difference procedure. After iteratively solving the discretized equations and validating the results using available literature data, a complete parametric study is done in order to find out the effects of the channel aspect ratio, the zeta potential, the dimensionless Debye-Hückel parameter, the Weissenberg number, and the velocity scale ratio on the hydrodynamic features of the flow.

2. Problem formulation

2.1. Problem definition

Consideration is given to combined electroosmotic and pressure driven flow of a viscoelastic fluid through a long rectangular microchannel with dimensions given in Figure 1. The rheological behavior of the fluid is assumed to be represented by either PTT or FENE-P models. The flow is considered to be steady, laminar, and fully developed. It is assumed that the liquid contains an ideal solution of fully dissociated symmetric salt. Moreover, the channel wall is considered to be subject to a constant zeta potential.

2.2. Electrical potential distribution

The electrostatic potential, φ , at any point in the channel will be described by superposition of the externally applied potential, Φ , along the channel axis, and the double layer potential, ψ . Under the hydrodynamically developed conditions $\psi = \psi(x, y)$, so:

$$\varphi(x, y, z) = \Phi(z) + \psi(x, y). \quad (1)$$

The electrostatic potential is related to the local net charge density, ρ_e , at certain point in the solution by the Poisson equation:

$$\nabla^2 \varphi = -\frac{\rho_e}{\varepsilon}, \quad (2)$$

where ε is the permittivity constant of the solution. In general, the Nernst-Planck equations should be used to relate the electric charge density to the electrostatic potential. However, at the hydrodynamically developed conditions, the spatial distribution of the electric

charge density is described by the Boltzmann equation, in spite of the fact that it assumes thermodynamic equilibrium [33]. This is due to the fact that, at the fully developed conditions, the velocity vector and the ion concentration gradient are orthogonal to each other. Using the Boltzmann distribution, the electric charge density for an ideal symmetric electrolyte of valence z is given by [34]:

$$\rho_e = -2ezn_0 \sinh\left(\frac{ez\psi}{k_B T}\right), \quad (3)$$

where n_0 is the ion density, e is the proton charge, k_B is the Boltzmann constant, and T is the absolute temperature. The introduction of the charge density expression into the Poisson equation along with the assumption of a constant voltage gradient in the z -direction results into the following modified version of Eq. (2):

$$\frac{\partial^2 \psi}{\partial x^2} + \frac{\partial^2 \psi}{\partial y^2} = \frac{2ezn_0}{\varepsilon} \sinh\left(\frac{ez\psi}{k_B T}\right), \quad (4)$$

which can be written in a dimensionless form as given below:

$$\frac{\partial^2 \Psi}{\partial X^2} + \frac{\partial^2 \Psi}{\partial Y^2} = K^2 \sinh(\Psi), \quad (5)$$

where $\Psi = ez\psi/k_B T$, $X = x/H$, $Y = y/H$, and $K = H/\lambda_D$ is the dimensionless Debye-Hückel parameter with $\lambda_D = (2n_0 e^2 z^2 / \varepsilon k_B T)^{-1/2}$ being the Debye length, a measure of the extent of EDL. The dimensionless electrical potential (Eq. (5)) is subject to the following boundary conditions:

$$\begin{aligned} \frac{\partial \Psi}{\partial X} \Big|_{X=0} &= \frac{\partial \Psi}{\partial Y} \Big|_{Y=0} = 0, \\ \Psi|_{X=\alpha} &= \Psi|_{Y=1} = Z, \end{aligned} \quad (6)$$

in which $Z = ez\zeta/k_B T$ is the dimensionless zeta potential and $\alpha = W/H$ stands for the channel aspect ratio.

2.3. Constitutive equations

The constitutive equation of PTT model, derived by Phan-Thien and Tanner [35] from network theory arguments, is given by:

$$\Pi(\tau_{kk})\boldsymbol{\tau} + \xi\boldsymbol{\tau}^\nabla = 2\mu\dot{\boldsymbol{\gamma}}, \quad (7)$$

where ξ is the relaxation time of the fluid and $\boldsymbol{\tau}^\nabla$ represents the upper convected derivative of the stress tensor $\boldsymbol{\tau}$, defined as:

$$\boldsymbol{\tau}^\nabla = \frac{D\boldsymbol{\tau}}{Dt} - \nabla\mathbf{u}^T \cdot \boldsymbol{\tau} - \boldsymbol{\tau} \cdot \nabla\mathbf{u}. \quad (8)$$

The stress coefficient function, $\Pi(\tau_{kk})$, is given by the linear form:

$$\Pi(\tau_{kk}) = 1 + \frac{\epsilon \xi}{\mu} \tau_{kk}, \tag{9}$$

where $\tau_{kk} = \tau_{xx} + \tau_{yy} + \tau_{zz}$ represents the trace of the stress tensor, and ϵ is a parameter that imposes an upper limit to the elongational viscosity.

The FENE-P model is based on the kinetic theory for finitely extensible dumbbells with a Peterlin approximation for the average spring force. For this model, the stress tensor is given by [36]:

$$\begin{aligned} \Pi(\tau_{kk})\boldsymbol{\tau} + \xi\boldsymbol{\tau}^\nabla - \xi \left(\boldsymbol{\tau} - \frac{b}{b+2}nk_B T\mathbf{I} \right) \frac{D \ln \Pi}{Dt} \\ = 2\mu \left(\frac{b+5}{b+2} \right) \dot{\boldsymbol{\gamma}}, \end{aligned} \tag{10}$$

where \mathbf{I} is the identity tensor, b is a parameter that measures the extensibility of the dumbbell, and n is a parameter of the model. Here, the stress coefficient function, $\Pi(\tau_{kk})$, is given by:

$$\Pi(\tau_{kk}) = 1 + 3 \left(\frac{1}{b+2} + \frac{\xi}{3\mu} \frac{\tau_{kk}}{b+5} \right). \tag{11}$$

For steady fully developed flow in ducts, the material derivatives of all the parameters vanish. Accordingly, the constitutive equation of FENE-P model is reduced to:

$$\Pi(\tau_{kk})\boldsymbol{\tau} + \xi\boldsymbol{\tau}^\nabla = 2\mu \left(\frac{b+5}{b+2} \right) \dot{\boldsymbol{\gamma}}. \tag{12}$$

By carefully inspecting Eqs. (7) and (9) and comparing them against Eqs. (12) and (11), respectively, it is revealed that at fully developed conditions, there is an exact equivalence of both PTT and FENE-P models equations in the sense of a parameter to parameter match, as explained by Afonso et al. [24]. Therefore, for convenience of analysis, it is useful to define generalized parameters and perform an analysis based on the generalized parameters instead of two analyses for both models. The following generalized parameters are introduced for the FENE-P model:

$$\Pi_{ge,FENE-P} = \left(\frac{b+5}{b+2} \right) \Pi, \tag{13}$$

$$\Pi_{ge,FENE-P} = \xi \left(\frac{b+5}{b+2} \right), \tag{14}$$

$$\epsilon_{ge,FENE-P} = \frac{1}{b+5}, \tag{15}$$

$$\mu_{ge,FENE-P} = \mu. \tag{16}$$

For PTT model, the generalized parameters are the same as those belonging to the model, i.e.:

$$\begin{aligned} \Pi_{ge,PTT} &= \Pi, & \xi_{ge,PTT} &= \xi, \\ \epsilon_{ge,PTT} &= \epsilon, & \mu_{ge,PTT} &= \mu. \end{aligned} \tag{17}$$

The generalized constitutive equations, therefore, become:

$$\Pi(\tau_{kk})\boldsymbol{\tau} + \xi_{ge}\boldsymbol{\tau}^\nabla = 2\mu_{ge}\dot{\boldsymbol{\gamma}}, \tag{18}$$

$$\Pi_{ge}(\tau_{kk}) = 1 + \frac{\epsilon_{ge} \xi_{ge}}{\mu_{ge}} \tau_{kk}. \tag{19}$$

2.4. Velocity distribution

Since the flow has been considered to be fully developed, the effects of transverse velocity components are neglected as compared to the axial component. Hence, the velocity vector becomes $\mathbf{u} = [0, 0, u(x, y)]$, resulting in the following rate of deformation tensor:

$$\dot{\boldsymbol{\gamma}} = \frac{1}{2} \begin{bmatrix} 0 & 0 & \frac{\partial u}{\partial x} \\ 0 & 0 & \frac{\partial u}{\partial y} \\ \frac{\partial u}{\partial x} & \frac{\partial u}{\partial y} & 0 \end{bmatrix}. \tag{20}$$

Also the upper convected derivative of $\boldsymbol{\tau}$ is obtained as:

$$\boldsymbol{\tau}^\nabla = - \begin{bmatrix} 2\tau_{xz} \frac{\partial u}{\partial x} & \tau_{xz} \frac{\partial u}{\partial y} + \tau_{yz} \frac{\partial u}{\partial x} & \tau_{zz} \frac{\partial u}{\partial x} \\ \tau_{xz} \frac{\partial u}{\partial y} + \tau_{yz} \frac{\partial u}{\partial x} & 2\tau_{yz} \frac{\partial u}{\partial y} & \tau_{zz} \frac{\partial u}{\partial x} \\ \tau_{zz} \frac{\partial u}{\partial y} & \tau_{zz} \frac{\partial u}{\partial y} & 0 \end{bmatrix}. \tag{21}$$

Substitution Eqs. (20) and (21) into Eq. (18) gives rise to the following stress components:

$$\tau_{xx} = \frac{2\xi_{ge}}{\mu_{ge}} \tau_{xz}^2, \quad \tau_{yy} = \frac{2\xi_{ge}}{\mu_{ge}} \tau_{yz}^2, \quad \tau_{zz} = 0, \tag{22}$$

$$\tau_{xz} = \frac{\mu_{ge}}{\Pi_{ge}} \frac{\partial u}{\partial x}, \quad \tau_{yz} = \frac{\mu_{ge}}{\Pi_{ge}} \frac{\partial u}{\partial y}. \tag{23}$$

In addition, combining Eqs. (19) and (22) gives:

$$\Pi_{ge}(\tau_{kk}) = 1 + 2 \frac{\epsilon_{ge} \xi_{ge}^2}{\mu_{ge}^2} (\tau_{xz}^2 + \tau_{yz}^2). \tag{24}$$

By substituting Eq. (23) into the momentum equation given by:

$$\rho \frac{D\mathbf{u}}{Dt} = \nabla p - \nabla \cdot \boldsymbol{\tau} + \mathbf{f}, \tag{25}$$

the following equation is obtained for the z -component of the momentum equation:

$$\begin{aligned} & \frac{\mu_{ge}}{\Pi_{ge}} \left(\frac{\partial^2 u}{\partial x^2} + \frac{\partial^2 u}{\partial y^2} \right) - \frac{\mu_{ge}}{\Pi_{ge}^2} \left(\frac{\partial \Pi_{ge}}{\partial x} \frac{\partial u}{\partial x} + \frac{\partial \Pi_{ge}}{\partial y} \frac{\partial u}{\partial y} \right) \\ &= \frac{\partial p}{\partial z} + 2E_Z e z n_0 \sinh \left(\frac{e z \psi}{k_B T} \right), \end{aligned} \tag{26}$$

where p shows the pressure, and the body force in the axial direction, f_z , has been replaced with $-2E_Z e z n_0 \sinh(ez\psi/k_B T)$ [21]. Eqs. (23), (24), and (26) may be written in dimensionless form as:

$$T_{xz} = \frac{1}{\Pi_{ge}} \frac{\partial U}{\partial X}, \quad T_{yz} = \frac{1}{\Pi_{ge}} \frac{\partial U}{\partial Y}, \tag{27}$$

$$\Pi_{ge} = 1 + 2 \epsilon_{ge} We^2 (T_{xz}^2 + T_{yz}^2), \tag{28}$$

$$\begin{aligned} & \frac{1}{\Pi_{ge}} \left(\frac{\partial^2 U}{\partial X^2} + \frac{\partial^2 U}{\partial Y^2} \right) - \frac{1}{\Pi_{ge}^2} \left(\frac{\partial \Pi_{ge}}{\partial X} \frac{\partial U}{\partial X} + \frac{\partial \Pi_{ge}}{\partial Y} \frac{\partial U}{\partial Y} \right) \\ &= -2\Gamma - \frac{K^2}{Z} \sinh(\Psi). \end{aligned} \tag{29}$$

The dimensionless parameters appeared in these equations are given as:

$$\begin{aligned} U &= u/u_{HS}, & u_{HS} &= -\epsilon \zeta E_Z / \mu_{ge}, \\ \Gamma &= u_{PD} / u_{HS}, & u_{PD} &= -H^2 (\partial p / \partial z) / 2\mu_{ge}, \\ T &= H\tau / \mu_{ge} u_{HS}, & We &= \xi_{ge} u_{HS} / H, \end{aligned} \tag{30}$$

where u_{PD} is the pressure driven velocity scale, u_{HS} is the Helmholtz-Smoluchowski electroosmotic velocity, and We is the Weissenberg number. The momentum equation is subject to the symmetry and no slip boundary conditions. The dimensionless forms of these boundary conditions are written as:

$$\left. \frac{\partial U}{\partial X} \right|_{X=0} = \left. \frac{\partial U}{\partial Y} \right|_{Y=0} = 0, \quad U|_{X=\alpha} = U|_{Y=1} = Z. \tag{31}$$

2.5. Flow parameters

Once the potential and velocity fields are obtained, the parameters of physical interest can be calculated. One of the important parameters of the hydrodynamics is the friction factor given as:

$$f = \frac{2\tau_{w,av}}{\rho u_{HS}}, \tag{32}$$

where $\tau_{w,av}$ is the average wall shear stress that can be obtained as:

$$\tau_{w,av} = -\frac{1}{W+H} \left(\int_0^W \tau_{yz}|_{y=H} dx + \int_0^H \tau_{xz}|_{x=W} dy \right). \tag{33}$$

Replacing the flow parameters with their non-dimensional forms, the friction factor in the form of the Poiseuille number is obtained as:

$$fRe = -\frac{2}{1+\alpha} \left(\int_0^\alpha T_{yz}|_{y=H} dX + \int_0^1 T_{xz}|_{X=\alpha} dY \right), \tag{34}$$

where $Re = \rho u_{HS} H / \mu_{ge}$.

The dimensionless mean velocity is also given as:

$$U_m = \frac{1}{\alpha} \int_0^1 \int_0^\alpha U dX dY. \tag{35}$$

3. Numerical procedure

Due to strong gradients near the wall, it is necessary to have smaller grid sizes in this region. Therefore, transformations are used to cluster the grid points near the channel wall. The X and Y coordinates are transformed into \hat{x} and \hat{y} as [37]:

$$\hat{x} = \ln \left(\frac{\beta + \frac{x}{W}}{\beta - \frac{x}{W}} \right) / \ln \left(\frac{\beta + 1}{\beta - 1} \right), \tag{36}$$

$$\hat{y} = \ln \left(\frac{\beta + \frac{y}{H}}{\beta - \frac{y}{H}} \right) / \ln \left(\frac{\beta + 1}{\beta - 1} \right), \tag{37}$$

where $H = H/H = 1$, $W = W/H = \alpha$, and β is the stretching parameter. With this transformation, the dimensionless forms of Eqs. (5), (27), and (29) can be rewritten in terms of \hat{x} and \hat{y} as:

$$\begin{aligned} & Q_1^2(\hat{x}) \frac{\partial^2 \Psi}{\partial \hat{x}^2} + Q_2(\hat{x}) \frac{\partial \Psi}{\partial \hat{x}} + Q_3^2(\hat{y}) \frac{\partial^2 \Psi}{\partial \hat{y}^2} \\ &+ Q_4(\hat{y}) \frac{\partial \Psi}{\partial \hat{y}} = K^2 \sinh \Psi, \end{aligned} \tag{38}$$

$$T_{xz} = \frac{Q_1(\hat{x})}{\Pi_{ge}} \frac{\partial U}{\partial \hat{x}}, \quad T_{yz} = \frac{Q_3(\hat{y})}{\Pi_{ge}} \frac{\partial U}{\partial \hat{y}}, \tag{39}$$

$$\begin{aligned} & \frac{1}{\Pi_{ge}} \left[Q_1^2(\hat{x}) \frac{\partial^2 U}{\partial \hat{x}^2} + Q_2(\hat{x}) \frac{\partial U}{\partial \hat{x}} + Q_3^2(\hat{y}) \frac{\partial^2 U}{\partial \hat{y}^2} \right. \\ &+ Q_4(\hat{y}) \frac{\partial U}{\partial \hat{y}} \left. \right] - \frac{1}{\Pi_{ge}^2} \left[Q_1^2(\hat{x}) \frac{\partial \Pi_{ge}}{\partial \hat{x}} \frac{\partial U}{\partial \hat{x}} \right. \\ &+ Q_3^2(\hat{y}) \frac{\partial \Pi_{ge}}{\partial \hat{y}} \frac{\partial U}{\partial \hat{y}} \left. \right] = -2\Gamma - \frac{K^2}{Z} \sinh(\Psi), \end{aligned} \tag{40}$$

where the functions $Q_{i=1...4}$ are given as:

$$\begin{aligned} Q_1(\hat{x}) &= \frac{e^{\Omega \hat{x}} + e^{-\Omega \hat{x}} + 2}{2\alpha \beta \Omega}, \\ Q_2(\hat{x}) &= \frac{e^{2\Omega \hat{x}} + 2e^{\Omega \hat{x}} - 2e^{-\Omega \hat{x}} - e^{-2\Omega \hat{x}}}{4\alpha^2 \beta^2 \Omega}, \end{aligned} \tag{41}$$

$$Q_3(\hat{y}) = \frac{e^{\Omega\hat{y}} + e^{-\Omega\hat{y}} + 2}{2\beta\Omega},$$

$$Q_4(\hat{y}) = \frac{e^{2\Omega\hat{y}} + 2e^{\Omega\hat{y}} - 2e^{-\Omega\hat{y}} - e^{-2\Omega\hat{y}}}{4\beta^2\Omega}, \quad (42)$$

where $\Omega = \ln[(\beta+1)/(\beta-1)]$. The associated boundary conditions are also transformed, accordingly. Since Eq. (28) does not include any of the x and y coordinates, it remains unchanged during the transformation process. Applying the central finite difference scheme, the discretized forms of Eqs. (38), (39), (28), and (40), developed for the inner points, become:

$$k_{0\psi}\Psi_{i,j} - k_{1\psi}\Psi_{i+1,j} - k_{2\psi}\Psi_{i-1,j}$$

$$= k_{3\psi}\Psi_{i,j+1}^g + k_{4\psi}\Psi_{i,j-1}^g, \quad (43)$$

$$T_{xz,i,j} = \frac{Q_1(\hat{x}_i)}{\Pi_{ge,i,j}^g} \frac{U_{i+1,j} - U_{i-1,j}}{2\Delta\hat{x}},$$

$$T_{yz,i,j} = \frac{Q_3(\hat{y}_i)}{\Pi_{ge,i,j}^g} \frac{U_{i,j+1} - U_{i,j-1}}{2\Delta\hat{y}}, \quad (44)$$

$$\Pi_{ge,i,j} = 1 + 2 \epsilon_{ge} We^2 (T_{xz,i,j}^2 + T_{yz,i,j}^2), \quad (45)$$

$$k_{0u}U_{i,j} - k_{1u}U_{i+1,j} - k_{2u}U_{i-1,j}$$

$$= k_{3u}U_{i,j+1}^g + k_{4u}U_{i,j-1}^g + k_{5u}. \quad (46)$$

The exact forms of the coefficients k_ψ and k_u are not shown here, in order to save space. Indices i and j denote the grid numbers in x and y directions, respectively. For the grids located on the boundaries, appropriate second order difference equations are used. Superscript g refers to the previous iteration results, while denoting guess values for the first iteration. The set of algebraic Eqs. (43) is solved by means of Tridiagonal Matrix Algorithm, considering the overall relative error of 10^{-7} . Afterward, a velocity distribution is guessed based on which the coefficients k_u which contain the guessed values of Π_{ge} are computed. Eq. (46) is then solved using TDMA solver and, after evaluating the shear stress components as well as $\Pi_{ge,i,j}$ from Eqs. (44) and (45), the new values are used to update the coefficients. This procedure continues until the required overall relative error of 10^{-7} is achieved. Once the velocity distribution is obtained, the flow parameters are evaluated by means of Cavalieri-Simpson method for integration.

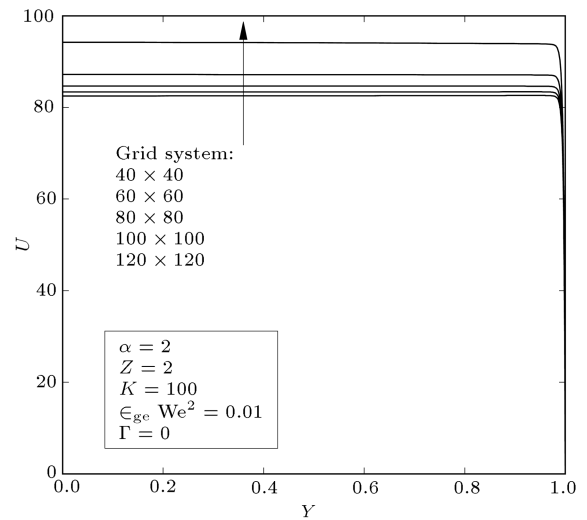


Figure 2. Grid dependency analysis of the velocity profile at the channel center.

4. Results and discussion

First of all, a mesh dependency analysis is performed to find out the minimum number of grid points that provides sufficiently accurate results. A mesh dependency of the velocity profile is performed in Figure 2. This figure shows that no significant change is occurred in the results by increasing the number of grid points in each direction from 100 to 120. More precisely, the difference between the maximum velocity values obtained by these grid systems is only about 1%. The dependency of the Poiseuille number on the number of grid points is also given in Table 1. When the number of grid points in each direction from 100 is increased to 120, only about 0.2% change is occurred in the Poiseuille number. Hence, it seems that a 120×120 grid system can provide sufficiently accurate results, especially because only the graphical data is presented here.

To estimate the value of $\epsilon_{ge} We^2$ for a typical microfluidic application, a channel height of $100 \mu\text{m}$ is considered. Moreover, the parameter ϵ_{ge} may be considered to be at most of the order 0.1, based on $\epsilon_{ge, FENE-P} = 1/(q + 5)$. Assuming an electroosmotic velocity of 1 mms^{-1} , the parameter $\epsilon_{ge} We^2$, then, will have a maximum value of 0.1 for $\xi_{ge} = 0.1$ [38]. The minimum value of $\epsilon_{ge} We^2$ is clearly zero, corresponding to a Newtonian behavior. Hence, the range 0-0.1 is considered for $\epsilon_{ge} We^2$.

For validation of the numerical method, the results are compared with existing literature data for

Table 1. Mesh dependency of the Poiseuille number values. Here, the flow parameters are the same as those of Figure 2.

Number of grid points	40 × 40	60 × 60	80 × 80	100 × 100	120 × 120
fRe	241.55	237.40	235.84	235.02	234.47

the limiting case of a parallel plate geometry. In this respect, the data reported by Afonso et al. [24] is chosen for comparison. A large aspect ratio of $\alpha = 50$ is considered here for the channel to imitate a slit, and the velocity profile across the channel height at the center of microchannel, that is $x = 0$, is chosen for a more reasonable comparison. Figure 3 shows the comparison between the velocity profiles obtained in the present study with those given by Afonso et al. [24]. As seen, a complete agreement is observed between the results. It should be pointed out that the definitions of the Weissenberg number, We , and the velocity scale ratio, Γ , in Ref. [24], are completely different from ours and

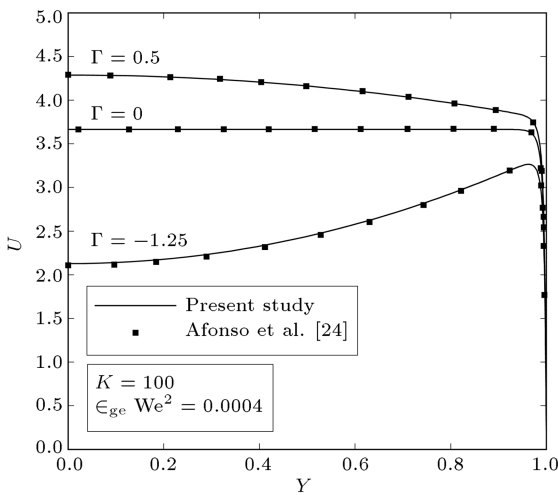


Figure 3. Comparison between the velocity profiles obtained in the present study at the limiting case of a parallel plate channel and those of Afonso et al. [24].

Table 2. Comparison between the present results and the results of Vakili et al. [21].

K	fRe		Discrepancy (%)
	Present study	Vakili et al. [21]	
5	8.7237	8.7264	0.031
10	18.7234	18.7267	0.018
50	98.7139	98.7263	0.013
100	198.6985	198.7268	0.014

we have therefore recalculated their data based on the present definitions.

The present Poiseuille numbers are also compared with the results of Vakili et al. [21] in Table 2. This comparison is done assuming a Newtonian fluid flow in a channel of square cross section. It can be seen that the results are in complete agreement; the maximum relative error is only about 0.03% which is quite reasonable.

The presentation of the results is continued by giving the distribution of U/U_m at different values of K for $\epsilon_{ge} We^2 = 0.1$ in Figure 4. It can be seen that for smaller values of K , such as $K = 5$, the velocity profile seems nearly parabolic and it becomes more plug-like as K increases. For $K = 5$, the EDL is relatively thick and the electric body force exists throughout the entire channel. Thus, the velocity variations exist in almost the whole channel domain, which results in a nearly parabolic profile. For higher values of K , such as $K = 100$, the EDL is confined to a thin layer near the wall. Therefore, the velocity variations exist only in this layer

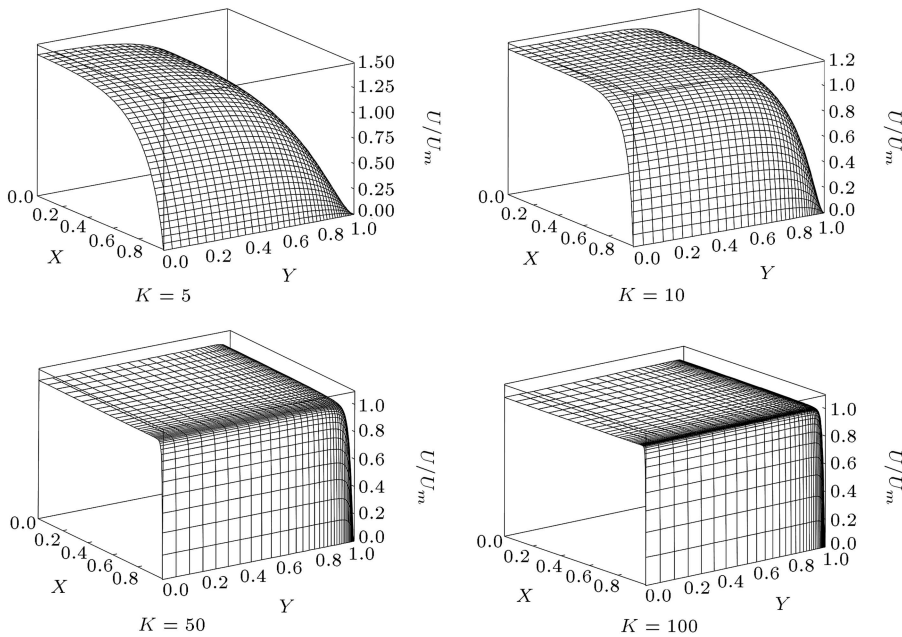


Figure 4. Distribution of U/U_m for purely electroosmotic flow in a square duct with $\epsilon_{ge} We^2 = 0.01$ and $Z = 2$ at different values of K .

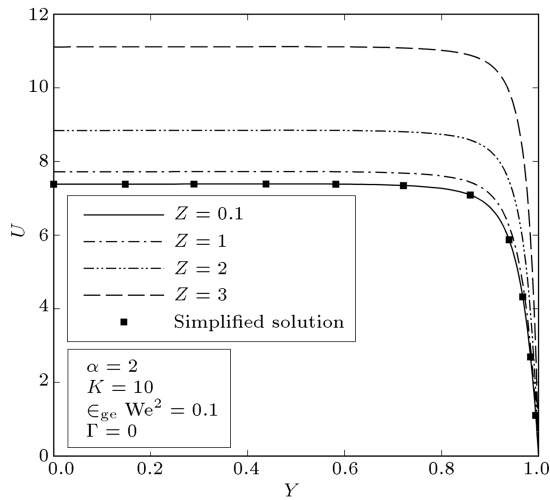


Figure 5. Dimensionless velocity at centerline for purely electroosmotic flow at different values of Z .

and the outside fluid is dragged by the fluid within EDL, creating a plug-like profile.

Figure 5 illustrates the profiles of the dimensionless velocity at centerline for purely electroosmotic flow of a viscoelastic fluid with $\epsilon_{ge} We^2 = 0.1$ at different zeta potentials. The predictions of the Debye-Hückel approximation, which are independent of Z , are also shown with symbols. As expected, an increase in zeta potential leads to an increase in the velocity, because of increasing the electroosmotic body force. Moreover, this figure reveals that the use of the Debye-Hückel linearization may lead to significant errors in predicting the electroosmotic velocity of viscoelastic fluids, as compared to the Newtonian fluids for which this validation is valid for $Z \leq 2$ [39]. However, Figure 6 shows that this linearization holds even at high zeta potentials, provided the velocity is normalized with the mean velocity. This means that, the Debye-Hückel linearization can approximately predict the shape of

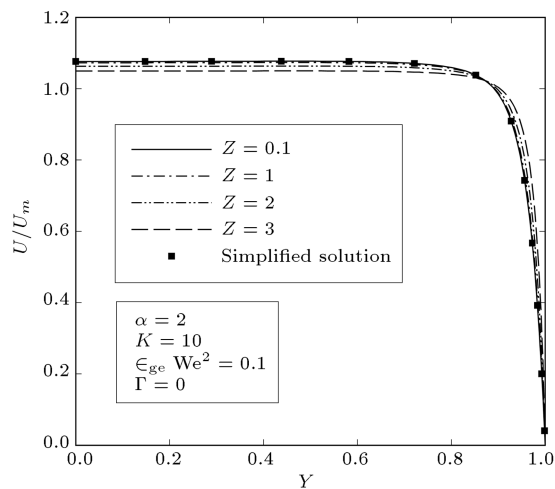


Figure 6. Normalized velocity at centerline for purely electroosmotic flow at different values of Z .

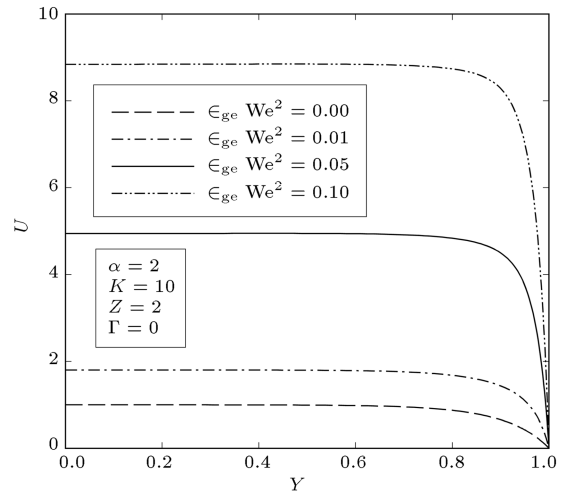


Figure 7. Velocity profile at centerline for purely electroosmotic flow at different levels of elasticity.

the velocity profile even at high zeta potentials, even though it fails to obtain the correct velocity magnitude.

The effect of elasticity, characterized by $\epsilon_{ge} We^2$, on the velocity profile, is observed in Figure 7. It is visible that elasticity effects drastically increase the fluid velocity. For a better evaluation of the elasticity effects, the normalized velocity at centerline for purely electroosmotic flow at different values of $\epsilon_{ge} We^2$ is given in Figure 8. As seen, an increase in $\epsilon_{ge} We^2$ gives rise to a more uniform velocity profile due to higher elasticity effects. In other words, fluid tends to behave more like a solid with the same velocities for its composed particles.

Figures 9 and 10 respectively depict the dimensionless mean velocity and Poiseuille number values versus K at different channel aspect ratios. It is observed that both of these parameters are increasing functions of K . The variations of fRe with K is expected because, as is clear from Figure 4, an increase

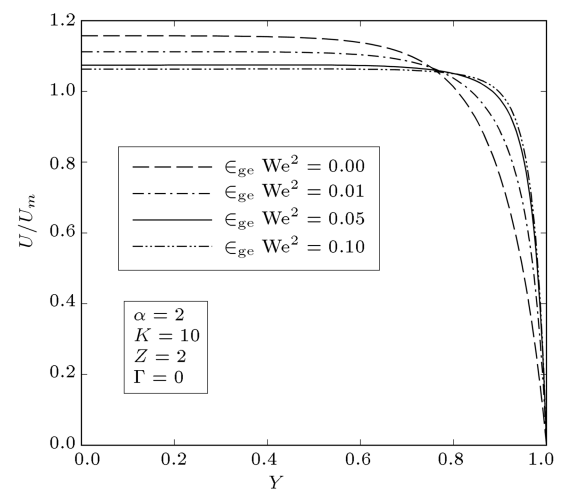


Figure 8. Normalized velocity at centerline for purely electroosmotic flow at different levels of elasticity.

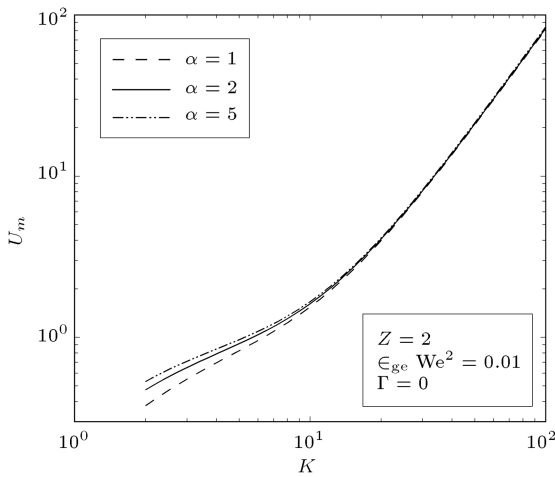


Figure 9. Dimensionless mean velocity versus the dimensionless Debye-Hückel parameter.

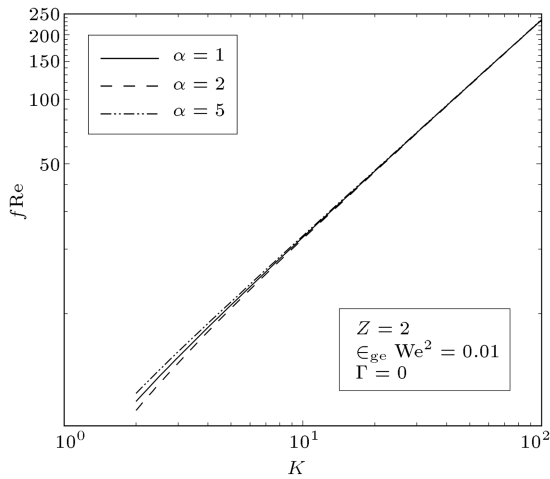


Figure 10. Poiseuille number versus the dimensionless Debye-Hückel parameter.

in this parameter gives rise to higher velocity gradients at the wall. However, at first glance, the variations of U_m with K seem to be odd as we would expect that the mean velocity would tend to an asymptotic value at high amounts of K . For interpretation of this odd behavior, let us assume that the Debye length remains unchanged while increasing K . Hence, for increasing K , the channel height should increase. Accordingly, for the Weissenberg number to remain unchanged, the relaxation time should increase. The increase in the relaxation time is to say that the level of elasticity is increased. As we saw, a higher level of elasticity is leading to higher velocities. Therefore, the velocity is an increasing function of K even at high values of this parameter. It is worth noting that by using the Debye length as the length scale in the definition of We the mean velocity will tend to an asymptotic value at high values of K [24]. It is also observed in Figure 9 that a higher channel aspect ratio results in a higher mean velocity. This is due

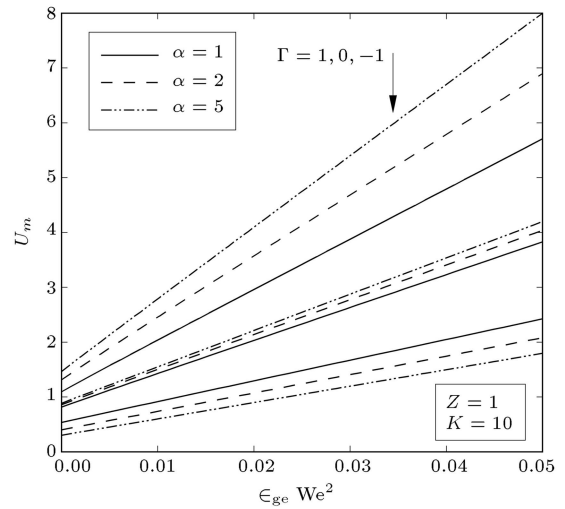


Figure 11. U_m versus $\epsilon_{ge} We^2$ at different values of α and Γ .

to the fact that, as the channel approaches a square shape, the corner effects become more prominent, leading to smaller amounts of the mean velocity. The aspect ratio dependency of the mean velocity vanishes at higher values of K due to the establishment of a nearly uniform velocity profile. The higher mean velocities for higher values of α , as expected, lead to higher Poiseuille numbers, as observed in Figure 10.

As the last illustration, the values of the dimensionless mean velocity are depicted versus $\epsilon_{ge} We^2$ in Figure 11. It can be seen that U_m is almost a linear increasing function of $\epsilon_{ge} We^2$, regardless of α and Γ . In addition, as expected, the mean velocity is an increasing function of the velocity scale ratio, because of increasing the pressure driving force. Another point taken from Figure 11 is that the pressure effects are more pronounced when the channel shape deviates from a rectangular geometry. As α increases the distance between the two vertical walls is increased for a given channel height, resulting in smaller surface effects at the channel center. This, in turn, prepares the way for a higher effect of the pressure force.

It is worth mentioning that the linearity of $U_m - \epsilon_{ge} We^2$ graph has an interesting outcome. It means that the velocity gradient at the wall is almost a linear function of $\epsilon_{ge} We^2$. Combining Eqs. (27) and (28) with the consideration of the fact that usually $\Pi_{ge} \gg 1$, due to huge values of stress near the wall for an electroosmotic flow, it can be concluded that both T_{xz} and T_{yz} at the wall are independent of $\epsilon_{ge} We^2$. This, according to Eq. (34), leads to the disappearance of the dependency of the Poiseuille number on the level of elasticity in the fluid. This conclusion is justified by our findings. The pertinent graphs are not shown here in order to save space.

5. Conclusions

In this paper, the viscoelasticity effects on fully developed electroosmotic flow in a rectangular microchannel were being investigated, utilizing both PTT and FENE-P constitutive equations. The problem was handled numerically, using a finite difference based method for a non-uniform grid. Instead of two separate analyses, an analysis was performed for both models, considering generalized parameters. The obtained results were validated using available literature data. A comprehensive parametric study showed that although the validity range of the Debye-Hückel linearization may be much narrower for viscoelastic fluids as compared to that of Newtonian fluids, however, this approximation holds even at high zeta potentials, provided the velocity is normalized with the mean velocity. It was also observed that the mean velocity is almost a linear function of the level of elasticity in the fluid. This linearity was found to lead to the disappearance of the dependency of the Poiseuille number on the level of elasticity in the fluid. Moreover, the pressure effects are pronounced when the channel shape deviates from a square geometry. Last but not least, both the mean velocity and Poiseuille number are increasing functions of the channel aspect ratio.

References

- Kirby, B.J., *Micro- and Nanoscale Fluid Mechanics; Transport in Microfluidic Devices*, Cambridge University Press, New York (2010).
- Reuss, F.F. "Charge-induced flow", *Proceedings of the Imperial Society of Naturalists of Moscow*, **3**, pp. 327-344 (1809).
- Diez, F.J., Hernaiz, G., Miranda, J.J. and Sureda, M. "On the capabilities of nano electrokinetic thrusters for space propulsion", *Acta Astronautica*, **83**, pp. 97-107 (2013).
- Sadeghi, A., Kazemi, Y. and Saidi, M.H. "Joule heating effects in electrokinetically driven flow through rectangular microchannels: An analytical approach", *Nanoscale and Microscale Thermophysical Engineering*, **17**, pp. 173-193 (2013).
- Burgreen, D. and Nakache, F.R. "Electrokinetic Flow in Ultrafine Capillary Slits", *Journal of Physical Chemistry*, **68**, pp. 1084-1091 (1964).
- Rice, C.L. and Whitehead, R. "Electrokinetic flow in a narrow cylindrical capillary", *Journal of Physical Chemistry*, **69**, pp. 4017-4024 (1965).
- Levine, S., Marriott, J.R., Neale, G. and Epstein, N. "Theory of electrokinetic flow in fine cylindrical capillaries at high zeta-potentials", *Journal of Colloid and Interface Science*, **52**, pp. 136-149 (1975).
- Tsao, H.-K. "Electroosmotic flow through an annulus", *Journal of Colloid and Interface Science*, **225**, pp. 247-250 (2000).
- Kang, Y., Yang, C. and Huang, X. "Electroosmotic flow in a capillary annulus with high zeta potentials", *Journal of Colloid and Interface Science*, **253**, pp. 285-294 (2002).
- Yang, D. "Analytical solution of mixed electroosmotic and pressure-driven flow in rectangular microchannels", *Key Engineering Materials*, **483**, pp. 679-683 (2011).
- Wang, C.Y., Liu, Y.H. and Chang, C.C. "Analytical solution of electro-osmotic flow in a semicircular microchannel", *Physics of Fluids*, **20**, p. 063105 (2008).
- Wang, C.Y. and Chang, C.C. "EOF using the Ritz method: Application to superelliptic microchannels", *Electrophoresis*, **28**, pp. 3296-3301 (2007).
- Goswami, P. and Chakraborty, S. "Semi-analytical solutions for electroosmotic flows with interfacial slip in microchannels of complex cross-sectional shapes", *Microfluidics and Nanofluidics*, **11**, pp. 255-267 (2011).
- Vocale, P., Geri, M., Morini, G.L. and Spiga, M. "Electro-osmotic flows inside triangular microchannels", *Journal of Physics: Conference Series*, **501**, 012026 (2014).
- Das, S. and Chakraborty, S. "Analytical solutions for velocity, temperature and concentration distribution in electroosmotic microchannel flows of a non-Newtonian bio-fluid", *Analytica Chimica Acta*, **559**, pp. 15-24 (2006).
- Zhao, C., Zholkovskij, E., Masliyah, J. and Yang, C. "Analysis of electroosmotic flow of power-law fluids in a slit microchannel", *Journal of Colloid and Interface Science*, **326**, pp. 503-510 (2008).
- Zhao, C. and Yang, C. "Nonlinear Smoluchowski velocity for electroosmosis of power-law fluids over a surface with arbitrary zeta potentials", *Electrophoresis*, **31**, pp. 973-979 (2010).
- Vasu, N. and De, S. "Electroosmotic flow of power-law fluids at high zeta potentials", *Colloids and Surfaces A: Physicochemical and Engineering Aspects*, **368**, pp. 44-52 (2010).
- Tang, G.H., Li, X.F., He, Y.L. and Tao, W.Q. "Electroosmotic flow of non-newtonian fluid in microchannels", *Journal of Non-Newtonian Fluid Mechanics*, **157**, pp. 133-137 (2009).
- Tang, G.H., Ye, P.X. and Tao, W.Q. "Pressure-driven and electroosmotic non-newtonian flows through microporous media via lattice Boltzmann method", *Journal of Non-Newtonian Fluid Mechanics*, **165**, pp. 1536-1542 (2010).
- Vakili, M.A., Sadeghi, A., Saidi, M.H. and Mozafari, A.A. "Electrokinetically driven fluidic transport of power-law fluids in rectangular microchannels", *Colloids and Surfaces A: Physicochemical and Engineering Aspects*, **414**, pp. 440-456 (2012).
- Park, H.M. and Lee, W.M. "Helmholtz-Smoluchowski velocity for viscoelastic electroosmotic flows", *Journal of Colloid and Interface Science*, **317**, pp. 631-636 (2008).

23. Dhinakaran, S., Afonso, A.M., Alves, M.A. and Pinho, F.T. “Steady viscoelastic fluid flow between parallel plates under electro-osmotic forces: Phan-Thien-Tanner model”, *Journal of Colloid and Interface Science*, **344**, pp. 513-520 (2010).
24. Afonso, A.M., Alves, M.A. and Pinho, F.T. “Analytical solution of mixed electro-osmotic/pressure driven flows of viscoelastic fluids in microchannels”, *Journal of Non-Newtonian Fluid Mechanics*, **159**, pp. 50-63 (2009).
25. Afonso, A.M., Pinho, F.T. and Alves, M.A. “Electro-osmosis of viscoelastic fluids and prediction of electro-elastic flow instabilities in a cross slot using a finite-volume method”, *Journal of Non-Newtonian Fluid Mechanics*, **179-180**, pp. 55-68 (2012).
26. Afonso, A.M., Alves, M.A. and Pinho, F.T. “Analytical solution of two-fluid electro-osmotic flows of viscoelastic fluids”, *Journal of Colloid and Interface Science*, **395**, pp. 277-286 (2013).
27. Sousa, J.J., Afonso, A.M., Pinho, F.T. and Alves, M.A. “Effect of the skimming layer on electro-osmotic-Poiseuille flows of viscoelastic fluids”, *Microfluidics and Nanofluidics*, **10**, pp. 107-122 (2011).
28. Bandopadhyay, A. and Chakraborty, S. “Electrokinetically induced alterations in dynamic response of viscoelastic fluids in narrow confinements”, *Physical Review E - Statistical, Nonlinear and Soft Matter Physics*, **85**, p. 056302 (2012).
29. Bandopadhyay, A. and Chakraborty, S. “Giant augmentations in electro-hydro-dynamic energy conversion efficiencies of nanofluidic devices using viscoelastic fluids”, *Applied Physics Letters*, **101**, p. 043905 (2012).
30. Bandopadhyay, A., Ghosh, U. and Chakraborty, S. “Time periodic electroosmosis of linear viscoelastic liquids over patterned charged surfaces in microfluidic channels”, *Journal of Non-Newtonian Fluid Mechanics*, **202**, pp. 1-11 (2013).
31. Ferrás, L.L., Afonso, A.M., Alves, M.A., Nóbrega, J.M. and Pinho, F.T. “Analytical and numerical study of the electro-osmotic annular flow of viscoelastic fluids”, *Journal of Colloid and Interface Science*, **420**, pp. 152-157 (2014).
32. Ghosal, S. “Lubrication theory for electro-osmotic flow in a microfluidic channel of slowly varying cross-section and wall charge”, *Journal of Fluid Mechanics*, **459**, pp. 103-128 (2002).
33. Park, H.M., Lee, J.S. and Kim, T.W. “Comparison of the Nernst-Planck model and the Poisson-Boltzmann model for electroosmotic flows in microchannels”, *Journal of Colloid and Interface Science*, **315**, pp. 731-739 (2007).
34. Probstein, R.F., *Physicochemical Hydrodynamics*, Wiley, New York (1994).
35. Thien, N.P. and Tanner, R.I. “A new constitutive equation derived from network theory”, *Journal of Non-Newtonian Fluid Mechanics*, **2**, pp. 353-365 (1977).
36. Bird, R.B., Dotson, P.J. and Johnson, N.L. “Polymer solution rheology based on a finitely extensible bead-spring chain model”, *Journal of Non-Newtonian Fluid Mechanics*, **7**, pp. 213-235 (1980).
37. Anderson, A., Tannehill, J.C. and Pletcher, R.H., *Computational Fluid Mechanics and Heat Transfer*, Hemisphere, Washington (1984).
38. Thurston, G.B. “Rheological parameters for the viscosity, viscoelasticity and thixotropy of blood”, *Biorheology*, **16**, pp. 149-162 (1979).
39. Sadeghi, A., Yavari, H., Saidi, M.H. and Chakraborty, S. “Mixed electroosmotically and pressure-driven flow with temperature-dependent properties”, *Journal of Thermophysics and Heat Transfer*, **25**, pp. 432-442 (2011).

Biography

Mohammad Mahdy Heydari is a Professor of Mechanical Engineering at Malek Ashtar University of Technology, Tehran, Iran. He received his BSc at Khajeh Nasiredin University of Technology, Tehran, Iran, in 1994, his MSc at Tarbiat Modares University, Tehran, Iran, in 1996 and his PhD at Sharif University of Technology, Tehran, Iran, in 2007, all in Mechanical Engineering. His research interests involve propulsion, combustion, heat transfer and renewable energy.